Pure and Applied Geophysics

CrossMark

Near-Source Strong Pulses During Two Large M_{JMA} 6.5 and M_{JMA} 7.3 Events in the 2016 Kumamoto, Japan, Earthquakes

KAZUHIRO SOMEI,[1] (iD) KEN MIYAKOSHI,[1] KUNIKAZU YOSHIDA,[1] SUSUMU KURAHASHI,[2] and KOJIRO IRIKURA[2]

Abstract—Extremely large ground motions with strong pulses were observed near source faults during two large M_{JMA} 6.5 and M_{JMA} 7.3 events of the 2016 Kumamoto earthquakes in Japan. To investigate the mechanisms for generation of near-source strong pulses during both events, we first performed strong ground motion simulations in a broadband frequency range between 0.2 and 10 Hz using the empirical Green's function method. For both the M6.5 and M7.3 events, strong motion generation area (SMGA) source models were prepared to simulate the ground motions, which were able to reproduce well the characteristics of the observed ground motions in and around the source areas. We also conducted ground motion simulations based on hypothetical simple source models to study the effect of rupture directivity on near-source strong ground motions. The principal findings regarding rupture directivity effects on near-source strong ground motions are as follows: (1) During the M6.5 event, the forward and upward rupture directivities from two strike-slip SMGAs caused two distinct strong pulses in the fault normal and parallel components, respectively. (2) During the M7.3 event, the upward rupture directivity along the fault dip direction from the strike-slip SMGA, including a small normal-slip, caused a strong pulse in both the fault parallel and normal components.

Key words: The 2016 Kumamoto earthquakes, rupture directivity effect, strong motion generation area, empirical Green's function method.

1. Introduction

Near-source strong ground motions during large inland crustal earthquakes, such as the 1994 Northridge and the 1995 Kobe earthquakes, have received considerable attention from the seismological and earthquake engineering communities because of their severe impact on urbanized areas. Following the developments of strong motion observational networks, many remarkable strong ground motions have been recorded during the last two or three decades, prompting studies of the generation mechanisms of near-source strong ground motions. Incorporating scientific knowledge on near-source ground motion generation into strong ground motion predictions of future earthquakes, we have been publishing seismic hazard maps and developing a methodology of design based on ground motions for important facilities.

After the M_{JMA} 6.5 inland crustal earthquake (hereafter the M6.5 event) occurred in Kumamoto prefecture, in central Kyushu Island, southwest Japan, at 21:26 (JST = UT + 9) on April 14, 2016, seismic activities have significantly increased in central Kyushu around Kumamoto prefecture, with a maximum M_{JMA} 7.3 event (hereafter the M7.3 event) that occurred at 01:25 on April 16, 2016 (Fig. 1). Based on the observational results from the aftershock distributions (e.g., Kato et al. 2016, Uchide et al. 2016), field surveys (e.g., Sugito et al. 2016, Shirahama et al. 2016) and ALOS-2/PALSAR-2 data (e.g., Ozawa et al. 2016, Fujiwara et al. 2016), these earthquakes (hereafter the 2016 Kumamoto earthquakes) mainly occurred along the Futagawa fault zone and the northern part of the Hinagu fault zone, referred to collectively as the Futagawa–Hinagu fault system, which is one of the major active right-lateral strike slip fault systems on Kyushu Island.

The Fire and Disaster Management Agency (2018) reported the 2016 Kumamoto earthquakes caused severe damage in and around the Kumamoto prefecture, centering on Mashiki, which is a typical residential area in Japan. More than 200 people were killed, including disaster-related deaths,

[1] Geo-Research Institute, 6F, Kokuminkaikan-Sumitomoseimei Bldg., 2-1-2, Otemae, Chuo-Ku, Osaka 540-0008, Japan. E-mail: somei@geor.or.jp
[2] Aichi Institute of Technology, 1247, Yachigusa, Yakusa Cho, Toyota, Aichi 470-0392, Japan.
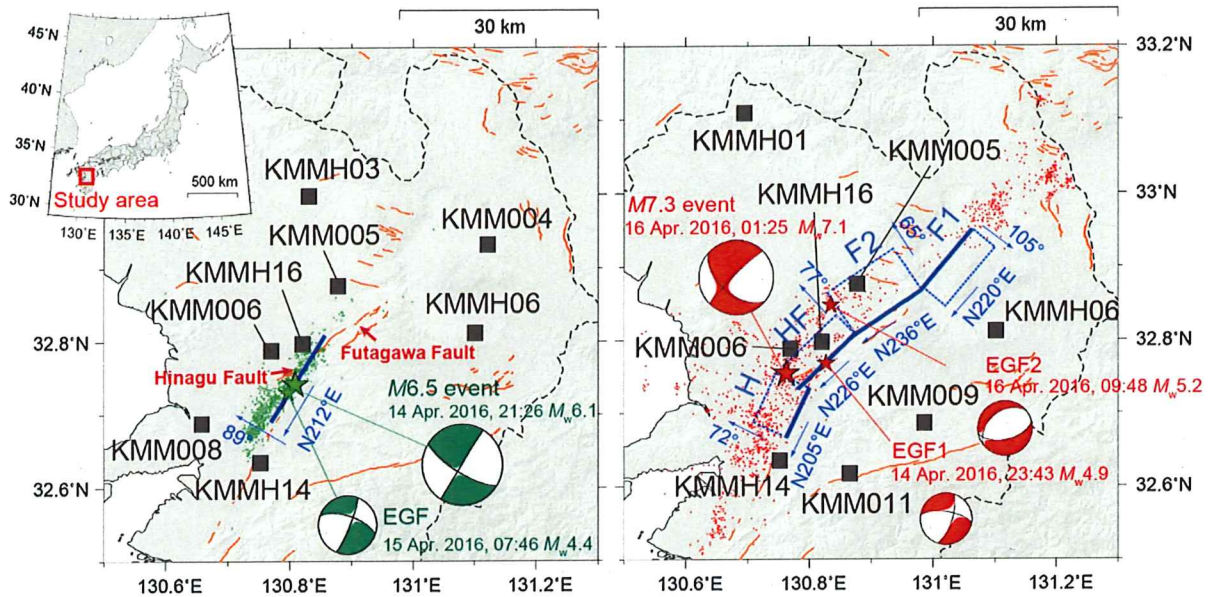
Birkhäuser

Figure 1

Map showing the study area. Squares indicate strong motion stations used in the ground motion simulations for each event. Orange lines represent surface traces of active faults compiled by Nakata and Imaizumi (2002). (Left) Epicenters of the *M*6.5 and EGF events with their moment tensor solutions determined by the broadband seismograph network F-net (Fukuyama et al. 1998). The blue rectangle (line) represents the surface projection of the assumed source fault plane of the *M*6.5 event based on the source inversion model by Yoshida et al. (2016). Green dots denote the epicenters of the events occurring in the period between the *M*6.5 and *M*7.3 events determined by JMA. (Right) Epicenters of the *M*7.3 and EGF events with their moment tensor solutions determined by F-net. Blue rectangles represent surface projections of the assumed source fault planes of the *M*7.3 event based on the source inversion model by Yoshida et al. (2017). Red dots denote the epicenters of the events occurring within 5 days after the *M*7.3 event determined by JMA

approximately 2800 were injured, and more than 8500 buildings completely collapsed. Two dense nationwide digital strong motion seismograph networks, K-NET and KiK-net, both installed and operated by the National Research Institute for Earth Science and Disaster Resilience, Japan (NIED) (Aoi et al. 2011), recorded the ground acceleration time histories with near-source strong ground motions during the 2016 Kumamoto earthquakes (Fig. 2). Figure 2 shows the large ground motions locally observed at stations more than 70 km northeast of the epicenter during the *M*7.3 event, which were attributed to the locally induced earthquake in the Oita region (Suzuki et al. 2017). For both the *M*6.5 and *M*7.3 events, extremely large ground motions with maximum peak ground accelerations (PGAs) greater than 1000 cm/s^2 were observed at KMMH16 station in Mashiki, the closest station to the source fault within the K-NET and KiK-net networks. KMMH16 is approximately 6 and 7 km from the epicenters of

the *M*6.5 and *M*7.3 events, respectively. Figure 3 shows the acceleration and velocity waveforms of the fault parallel (FP) and normal (FN) components observed by the surface and downhole sensors at KMMH16 during the *M*6.5 and *M*7.3 events, respectively. The extremely high accelerations seen only on the ground surface at KMMH16 were remarkably amplified by soft layers near the surface (e.g., Kobayashi et al. 2017b; Kurita 2017). The peak ground accelerations and peak ground velocities within the K-NET and KiK-net networks for both the *M*6.5 and *M*7.3 events generally followed the ground motion prediction equations by Si and Midorikawa (1999), popularly referenced in Japan (Suzuki et al. 2017). On the other hand, velocity pulses were seen in both the surface and downhole data at KMMH16: For the *M*6.5 event, two velocity pulses were observed in the FP and FN components, also for the *M*7.3 event, a large velocity pulse was observed in the FP component as well as the FN component.
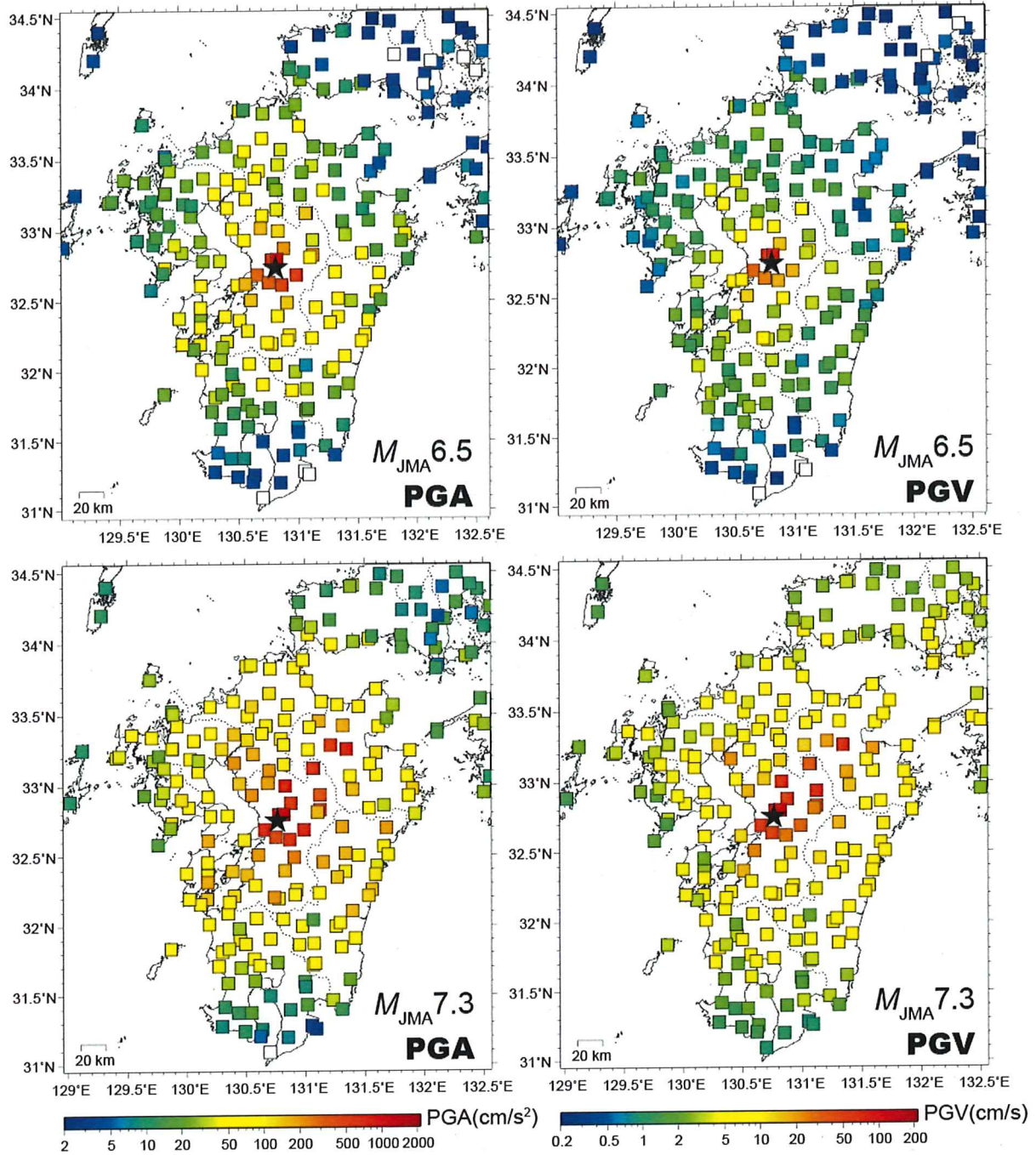
Figure 2
Spatial distributions of PGA (left) and PGV (right) for the K-NET and KiK-net stations. Upper and lower panels indicate the M6.5 and M7.3 events, respectively. Stars denote the epicenters for each event

To better understand the physical mechanisms of the ground motion generation processes and/or surface ruptures during the 2016 Kumamoto earthquakes, mainly for the M7.3 event, kinematic heterogeneous slip histories of the source faults have been estimated in space and in time using inversion
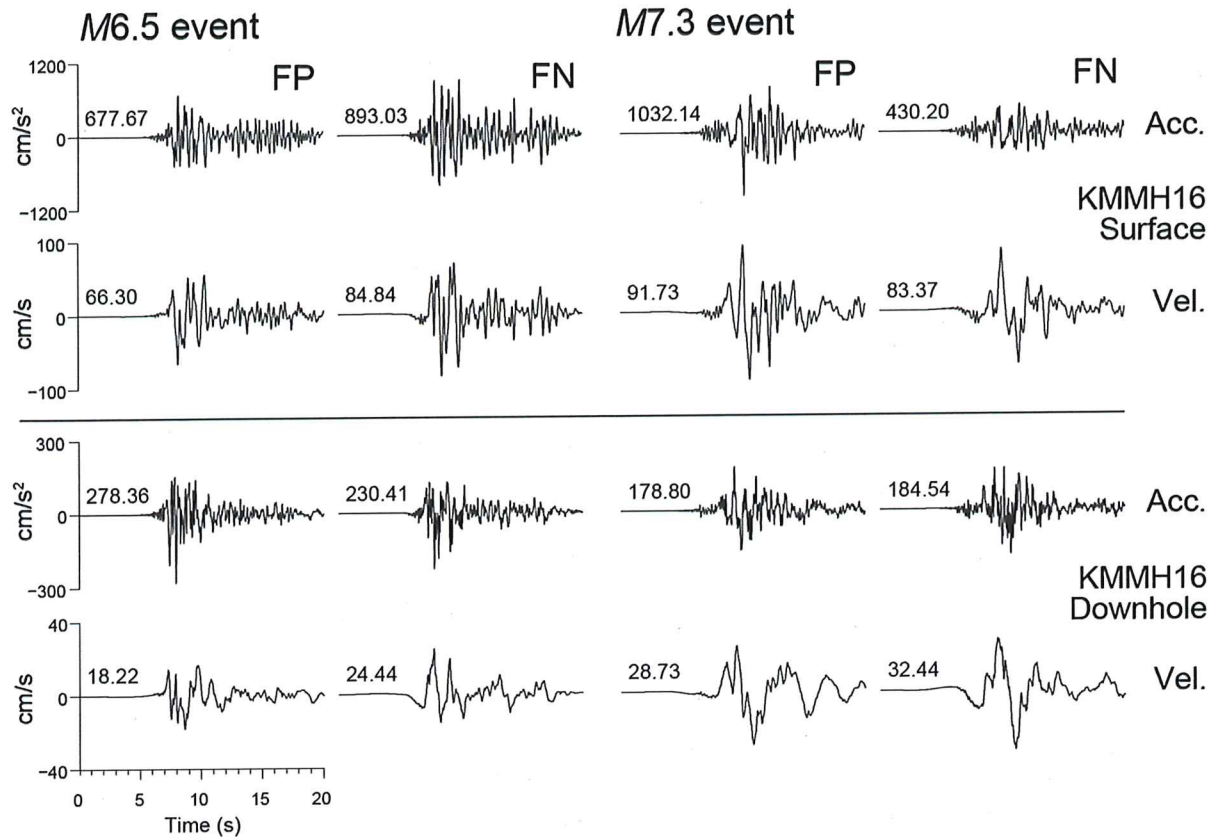
Figure 3
Acceleration and velocity waveforms observed from 0.2 to 10 Hz at KMMH16 during the M6.5 (Left) and M7.3 (Right) events. FP and FN are the fault parallel and fault normal components according to the fault strike angle of N212°E for the M6.5 event and N226°E for the M7.3 event. Upper and lower panels represent the waveforms recorded at the surface and downhole sensors, respectively. Depth of the downhole sensor at KMMH16 was 252 m. The maximum amplitude of the waveforms is shown above each trace

analyses of teleseismic data (e.g., Yagi et al. 2016); strong motion data (e.g., Asano and Iwata 2016, Kubo et al. 2016, Yoshida et al. 2017); both teleseismic and strong motion data (e.g., Hao et al. 2017); and combined datasets from teleseismic, strong motion, and geodetic data (e.g., Kobayashi et al. 2017a). However, these studies used the ground motion data in a frequency range lower than 1 Hz. To account for observed strong ground motions in a broadband frequency range, including frequencies higher than 1 Hz, which are indispensable in terms of seismic damage on buildings and civil structures, Irikura et al. (2017) constructed a source model consisting of Strong Motion Generation Areas (SMGAs: Miyake et al. 2003), which are defined as high slip velocity or large stress drop areas on the source fault. They used the empirical Green's function (EGF) method (e.g., Irikura 1986), which uses the records of small events occurring near the target event as empirical Green's functions to simulate the ground motions in a broadband frequency range between 0.2 and 10 Hz. They indicated the applicability of a scaling relationship for inland crustal earthquakes in Japan to explain the ground motions during the M7.3 event in the 2016 Kumamoto earthquakes.

One of the essential questions raised by the 2016 Kumamoto earthquakes is how the near-source strong ground motions with strong velocity pulses at KMMH16 were generated during both the M6.5 and M7.3 events. To address this question, source models that can reliably explain observed broadband ground

motions in and around the source areas are necessary. For both the M6.5 and M7.3 events, which resulted in extreme ground motion with strong velocity pulses near the source faults, this study focused on SMGA source models. For the M6.5 event, we originally estimated a two-SMGA model using broadband ground motion simulations at K-NET and KiK-net stations and the EGF method. For the M7.3 event, a three-SMGA model constructed by Irikura et al. (2017) was used for simulating the ground motions. In the following sections, we first describe the source models and strong ground motion simulations for both the M6.5 and M7.3 events. Then, we discuss the mechanisms generating strong pulses at the near-source station KMMH16 during both events.

2. Dataset

Figure 1 shows the spatial distribution of the strong motion stations of the K-NET and KiK-net stations used in this study. The location of each station is listed in Table 1. For both the M6.5 and M7.3 events, four K-NET and four KiK-net stations were used. The downhole records of the KiK-net stations installed in the basement rock were mostly used to avoid the soil nonlinearity effects of superficial layers during strong ground motions. The original records were the three components of the acceleration time histories sampled at 100 Hz for the K-NET and KiK-net stations. All the observed acceleration waveform

data were band-pass filtered between 0.2 and 10 Hz using a Chebyshev Type I recursive filter.

3. SMGA Source Models and Strong Ground Motion Simulations

3.1. Empirical Green's Function Method

The EGF method originally proposed by Irikura (1986) is a technique used to synthesize seismic records by summing the observed records of small earthquakes as empirical Green's functions. In general, calculating a Green's function from source to station, which explains the higher frequency range, is difficult, because one does not know the detailed three-dimensional (3D) underground structure. From this point of view, a clear advantage of the EGF method is that we directly know the Green's function using the observed records of small earthquakes. Hereafter we term a small earthquake an "EGF event."

The synthetic time-series waveform record of the target event $U(t)$ is expressed as a superposition of the records of an EGF event $u(t)$ using a filtering function $F(t)$, which adjusts the slip time function of the EGF event to that of the target event (Irikura 1986, Irikura et al. 1997) as follows:

$$U(t) = \sum_{i=1}^{N} \sum_{j=1}^{N} \frac{r}{r_{ij}} \{F(t) * (C \cdot u(t))\}, \qquad (1)$$

Table 1

Station list used in this study

Station code	Latitude (°N: WGS)	Longitude (°E: WGS)	Network	Location	M6.5 event[*1]	M7.3 event[*1]
KMM004	32.9320	131.1214	K-NET	Ichinomiya	○	
KMM005	32.8761	130.8774	K-NET	Ohdu	○	○
KMM006	32.7934	130.7772	K-NET	Kumamoto	○	○
KMM008	32.6878	130.6582	K-NET	Uto	○	
KMM009	32.8267	131.1226	K-NET	Yabe		○
KMM011	32.6167	130.8652	K-NET	Tomochi		○
KMMH01	33.1089	130.6949	KiK-net	Kahoku		○
KMMH03	32.9984	130.8301	KiK-net	Kikuchi	○	
KMMH06	32.8114	131.1010	KiK-net	Hakusui	○	○
KMMH14	32.6345	130.7521	KiK-net	Toyono	○	○
KMMH16	32.7967	130.8199	KiK-net	Mashiki	○	○

*1 Indication used for each event

$$F(t) = \delta\left(t - t_{ij}\right) + \frac{1}{n'(1 - e^{-1})}$$
$$\cdot \sum_{k=1}^{(N-1)n'} \left[e^{-\frac{k-1}{(N-1)n'}} \delta\left\{ t - t_{ij} - \frac{(k-1)\tau}{(N-1)n'} \right\} \right],$$

$$(2)$$

$$t_{ij} = \frac{r_{ij} - r_0}{\beta} + \frac{\xi_{ij}}{V_R}, \qquad (3)$$

where τ is the rise time for the target event, n' is the integer to shift artificial periodicity outside of the analyzing frequency range, β is the S-wave velocity around the source region, and V_R is the rupture velocity. ξ_{ij} is the distance between the subfault (i, j) and the rupture starting point of the target event; r_0 and r are the hypocentral distances of the target and the EGF events, respectively; and N and C are the ratios of the source dimensions and the stress drops between the target and EGF events, respectively.

Two scaling parameters, N and C, which are necessary in the EGF method as introduced in Eqs. (1) and (2), can be expressed in the following relationships:

$$\frac{U_0}{u_0} = \frac{M_0}{m_0} = CN^3, \qquad (4)$$

$$\frac{A_0}{a_0} = CN, \qquad (5)$$

where U_0 and u_0 are the flat levels in the lower frequency limit of the displacement source spectra for the target and EGF event, respectively, M_0/m_0 is the seismic moment ratio between the target and EGF event, and A_0 and a_0 are the flat levels in the high frequency limit of the acceleration source spectra for the target and EGF event, respectively.

In this study, we generally followed the procedures of Miyake et al. (2003) to determine these parameters by fitting the observed source spectral ratio between the target and EGF events to the theoretical source spectral ratio following the ω^{-2} source spectral model. The moment ratio was provided by the seismic moments obtained from the moment tensor solutions by F-net. The corner frequencies for the target and EGF events were estimated using a grid search algorithm. First, the observed source spectral ratio for each station was calculated from the Fourier amplitude spectra of the

direct S-wave portion, correcting for the propagation path effects for geometrical spreading of the body waves and an attenuation factor. The frequency-dependent quality factor for the S-wave $Q_S = 62f^{0.87}$ obtained by Satoh (2016) in this region was used to correct for the attenuation factor. The S-wave velocity was assumed to be 3.4 km/s based on the Japan Seismic Hazard Information Station (J-SHIS) for deep sedimentary layers model V2 (hereafter the "J-SHIS model"), which is a nation-wide 3D velocity structure model from the seismic bedrock to the engineering bedrock (Fujiwara et al. 2009, 2012).

3.2. SMGA Model for the M6.5 Event

For modeling the SMGA of the $M6.5$ event, we used records of an M_w 4.4 aftershock whose source parameters are listed, together with those of the $M6.5$ event, in Table 2. The EGF event had a focal mechanism similar to that of the $M6.5$ event and occurred to the southwest near the epicenter of the $M6.5$ event (Fig. 1). From the observed waveforms at KMMH16 during the $M6.5$ event, as shown in Fig. 3, we can see that S-wave portion consists mainly of two wave packets. These two S-wave packets were clearly observed in the records at the strong motion stations surrounding the source area. Therefore, we assumed two squared SMGAs on the source fault using the same hypocenter location and fault geometry as those used in Yoshida et al. (2016), shown in Fig. 1.

Figure 4 shows the observed source spectral ratio, which was obtained from the strong motion records at the KiK-net and F-net stations, with the theoretical ω^{-2} source spectral ratio model estimated via the grid search. From the corner frequencies and seismic moments, considered with the partition coefficient in the case of the multi-SMGA model (Miyake et al. 2003), we first estimated the N and C for each SMGA as the initial values. Based on these initial values, N and C for each SMGA were commonly determined as 4 and 1.50, respectively, by waveform fitting in observations and simulations of the $M6.5$ event.

We performed ground motion simulations in the broadband frequency range from 0.2 to 10 Hz, depending on the signal-to-noise ratio of the records for the EGF event, to construct the SMGA model for

Table 2

Source parameters of the M6.5 event and the EGF event

	*M*6.5 event	EGF event
Origin time (JST = UT + 9)[*1]	14 Apr 2016, 21:26	15 Apr 2016, 07:46
Epicentral latitude[*1]	32.7417°N	32.7300°N
Epicentral longitude[*1]	130.8087°E	130.7970°E
Hypocentral depth[*1]	11.39 km	10.52 km
Focal mechanism (strike, dip, rake)[*2]	(212, 89, − 164)	(22, 82, − 155)
Seismic moment (M_w)[*2]	1.74×10^{18} Nm (6.1)	4.19×10^{15} Nm (4.4)

[*1]Japan Meteorological Agency (JMA)

[*2]F-net
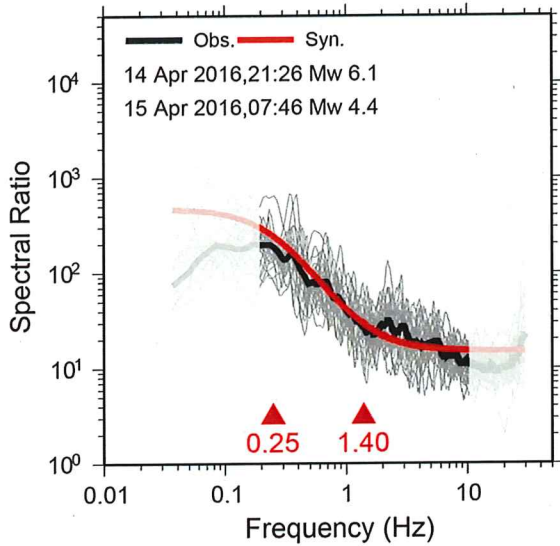
Figure 4

Observed source spectral ratios for each station (thin gray lines), average observed source spectral ratios among stations (thick black line), and theoretical source spectral ratio (red line) fitted to the observation. Solid triangles indicate the corner frequencies for the *M*6.5 and EGF events, respectively

the *M*6.5 event. Six parameters for the SMGAs representing the size (length and width), position (rupture starting point), rise time, rupture velocity, and stress drop, were estimated by minimizing the residuals of both the acceleration envelope and displacement waveform fittings between the observations and simulations for 20 s, including the *S*-wave portions in the three components. The fitting was completed by forward modeling using a trial and error method. Following this approach, we estimated
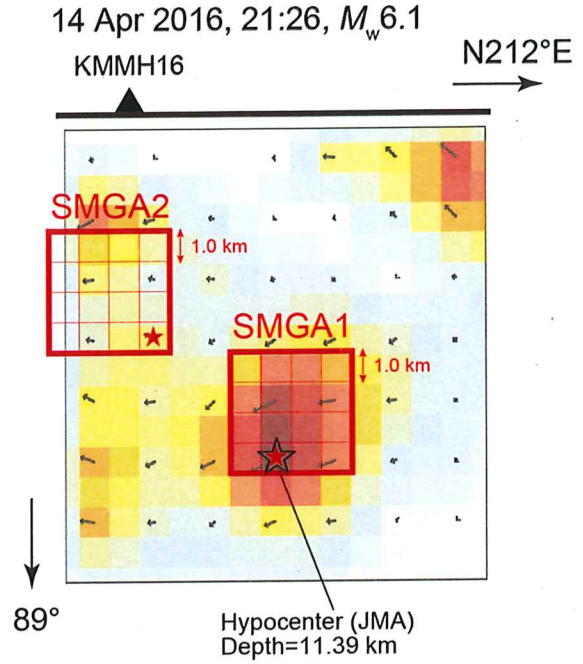

Figure 5

SMGA source model and slip distribution deduced by Yoshida et al. (2016) for the *M*6.5 event. Red rectangles are the estimated SMGA with red stars indicating the rupture starting point. The black open star is the hypocenter of the *M*6.5 event

SMGAs for the *M*6.5 event as shown in Fig. 5. The estimated parameters of the SMGAs are listed in Table 3. The two SMGAs were located near the large slip areas of the kinematic source model by Yoshida et al. (2016); one was found near the hypocenter, and the other was identified at a shallow depth along the northeastern side of the hypocenter, which is immediately beneath Mashiki. The simulated acceleration and velocity waveforms radiated from two SMGAs could reproduce the observations in and around the source area (Fig. 6). The estimated stress drop of both

Table 3

Estimated parameters of the SMGAs for the M6.5 event

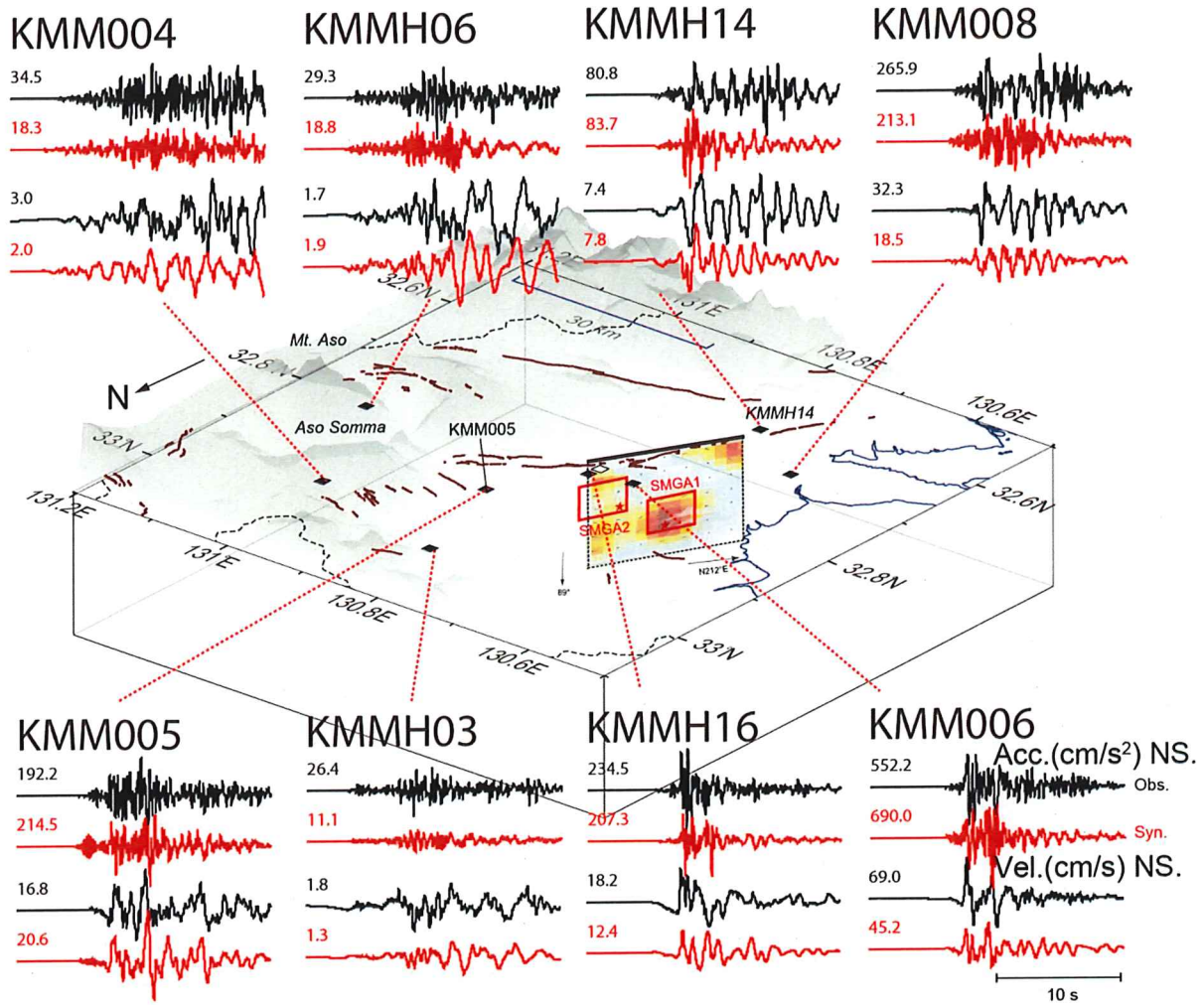|		SMGA1	SMGA2
Length	L (km)	4.0	4.0
Width	W (km)	4.0	4.0
Area	S (km²)	16.0	16.0
Rise time	τ (s)	0.24	0.40
Seismic moment	M_0 (Nm)	4.02×10^{17}	4.02×10^{17}
Stress drop	$\Delta\sigma$ (MPa)	15.3	15.3
Rupture velocity	V_r (km/s)	2.8	2.8

Figure 6
Birds eye view of the source model for the *M*6.5 event. Red rectangles on the slip model by Yoshida et al. (2016) represent the SMGAs. Rupture starting point of each SMGA is indicated by the red star. Black squares show the strong motion stations with observed (black) and simulated (red) acceleration and velocity waveforms in the N–S component (0.2–10 Hz), respectively. The maximum amplitude of the waveforms is shown above each trace in cm/s^2 and cm/s, respectively

Table 4

Source parameters of the M7.3 event and the EGF event

|	*M*7.3 event	EGF1 event	EGF2 event
Origin time (JST = UT + 9)[*1]	16 Apr 2016, 01:25	14 Apr 2016, 23:43	16 Apr 2016, 09:48
Epicentral latitude[*1]	32.7545°N	32.7670°N	32.8470°N
Epicentral longitude[*1]	130.7630°E	130.8273°E	130.8350°E
Hypocentral depth[*1]	12.45 km	14.20 km	15.91 km
Focal mechanism (strike, dip, rake)[*2]	(226, 84, − 142)	(279, 67, − 22)	(230, 38, − 112)
Seismic moment (M_w)[*2]	4.42 × 10^{19} Nm (7.1)	2.71 × 10^{16} Nm (4.9)	6.27 × 10^{16} Nm (5.2)

[*1]JMA

[*2]F-net
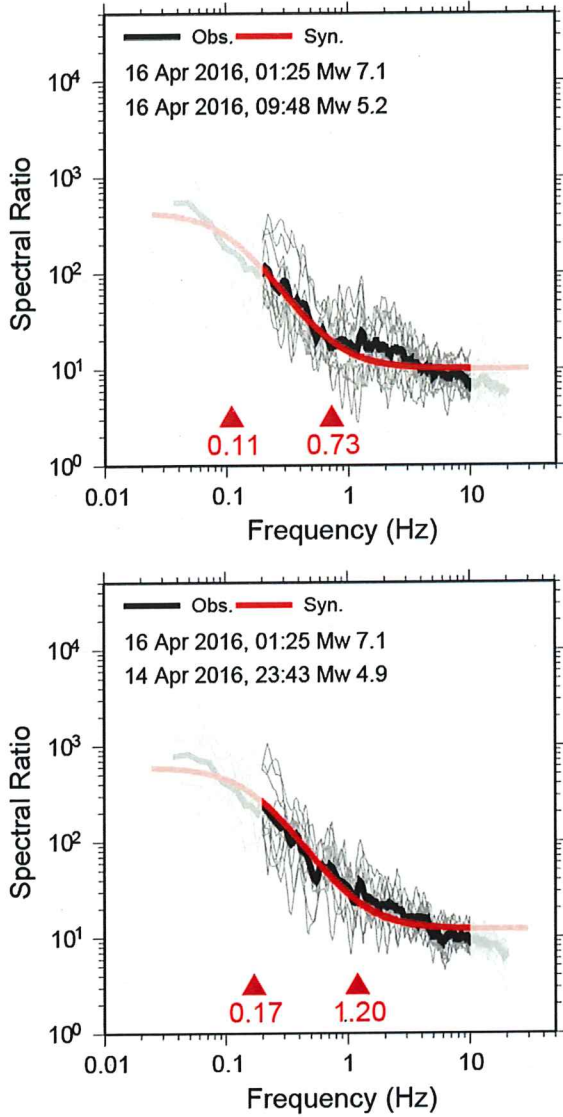
Figure 7

Observed source spectral ratios for each station, average observed source spectral ratios among stations, and theoretical source spectral ratio fitted to the observation. Solid triangles indicate the corner frequencies for the M7.3 and EGF events, respectively. The line colors are the same as those shown in Fig. 4

SMGAs was 15.3 MPa, which is comparable to the averaged value of past large inland crustal earthquakes in Japan.

3.3. SMGA Model for the M7.3 Event

Irikura et al. (2017) constructed an SMGA source model for the M7.3 event using broadband strong ground motion simulations from 0.2 to 10 Hz and the EGF method. Their three-SMGA model was estimated on the multi-segment fault model setting along the Futagawa–Hinagu fault system by Yoshida et al. (2016), whose fault geometries are shown in Fig. 1. Figure 1 also shows the epicenters of the M7.3 event and two EGF events with their F-net moment tensor solutions. The source parameters of these events are listed in Table 4. The scaling parameters N and C for each SMGA were determined by the same procedure introduced in the previous section. Figure 7 shows the fitting between the observed and theoretical source spectral ratios. Figure 8 shows the SMGA model, whose parameters are listed in Table 5, and the spatial slip distribution from the kinematic heterogeneous source model by Yoshida et al. (2016). The rupture inside SMGA1 propagated in a southwest direction from the hypocenter of the M7.3 event. SMGA2 was located immediately beneath KMMH16 and its rupture propagated mainly in the up-dip direction. The rupture inside SMGA3 propagated in a northeast direction. The stress drops of the SMGA1, 2, and 3 were 13.6, 13.6, and 13.4 MPa, respectively, comparable to the averaged values of past large inland crustal earthquakes in Japan.

In this study, ground motion simulations for the M7.3 event were conducted based on this three-SMGA model. Figure 9 shows a comparison of acceleration and velocity waveforms between observations and simulations in the E–W component at the strong motion stations surrounding the source area. Although simulations satisfactorily explained the main characteristics of the observed waveforms for most of the stations, some discrepancies can be seen along the northeast side of the source fault. Scope remains to improve the parameters of the SMGA in the Futagawa fault segment, which assesses the ground motions along the northeast side of the source fault.

4. Discussion

To elucidate the mechanisms generating strong pulses at the near-source station KMMH16 during both the M6.5 and M7.3 events, we first discuss the observed and simulated velocity waveforms at KMMH16 during both events, focusing on the
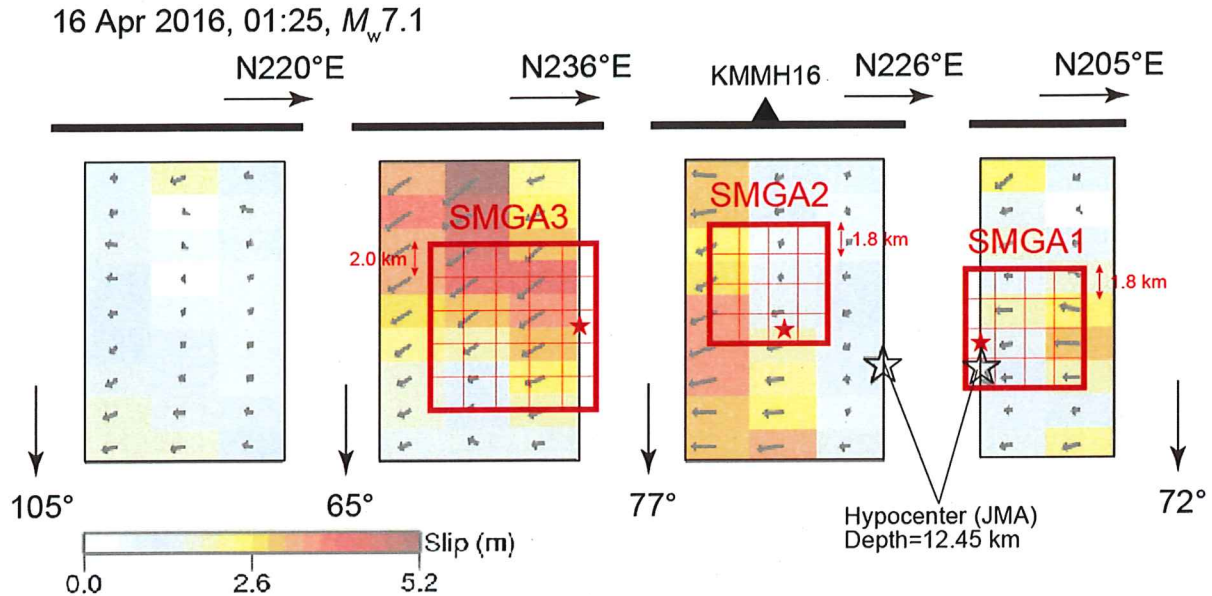
Figure 8
Three-SMGA source model by Irikura et al. (2017) and the spatial slip distribution along the source fault from the kinematic inversion model by Yoshida et al. (2017) for the *M*7.3 event. Red rectangles are the estimated SMGA with red stars indicating the rupture starting point. The black open star is the hypocenter of the *M*7.3 event

Table 5

Estimated parameters of the SMGAs for the M7.3 event

		SMGA1	SMGA2	SMGA3
Length	L (km)	7.2	7.2	10.0
Width	W (km)	7.2	7.2	10.0
Area	S (km²)	51.8	51.8	100.0
Rise time	τ (s)	0.6	0.6	0.6
Seismic moment	M_0 (Nm)	2.08×10^{18}	2.08×10^{18}	5.49×10^{18}
Stress drop	$\Delta\sigma$ (MPa)	13.6	13.6	13.4
Rupture velocity	V_r (km/s)	2.8	2.8	2.8
EGF event	–	EGF1	EGF1	EGF2

contributions of each SMGA and the rupture directions to the strong pulses. We also demonstrate a set of simple ground motion simulations to discuss the importance of rupture direction inside the SMGA in a strong pulse near the source fault.

4.1. Observed and Simulated Waveforms at KMMH16

To investigate the difference between the up-dip and down-dip rupture directivity effects on the simulated waveform at KMMH16, the two rupture cases with different rupture starting points during the

*M*6.5 and *M*7.3 events are shown in Fig. 10a and b, respectively. Velocity waveforms for those models were simulated in the range from 0.2 to 10 Hz using the EGF method. From the contributions of each SMGA to the simulated waveforms at KMMH16, we discuss the rupture directivity effects from SMGA1 and 2 for the *M*6.5 event and from SMGA2 for the *M*7.3 event to the simulations. The rupture in Case A, which is the original case as shown in the previous sections, is mainly propagated in the up-dip direction inside those SMGAs of both events, whereas the rupture in Case B is mainly propagated in the down-dip direction.
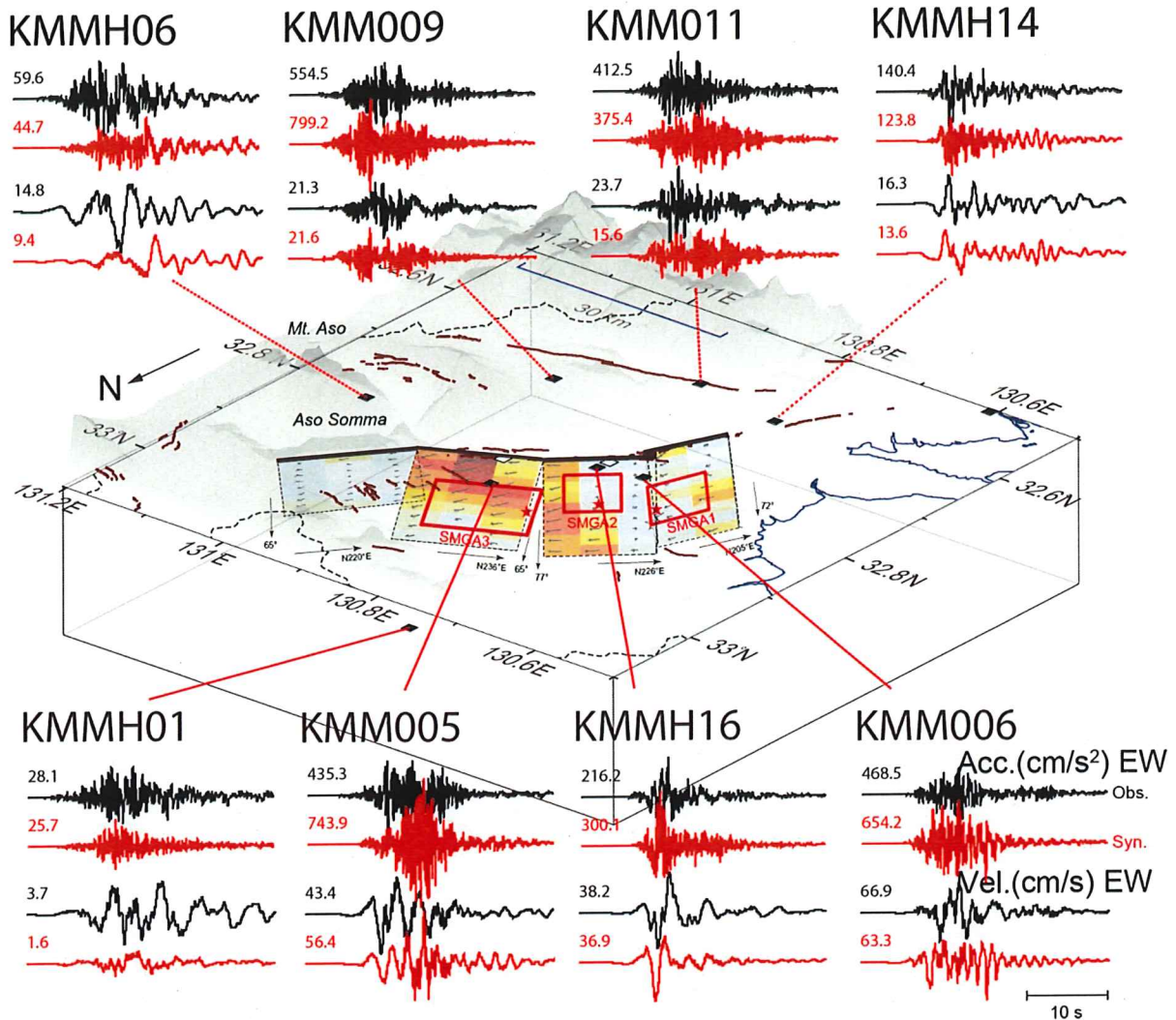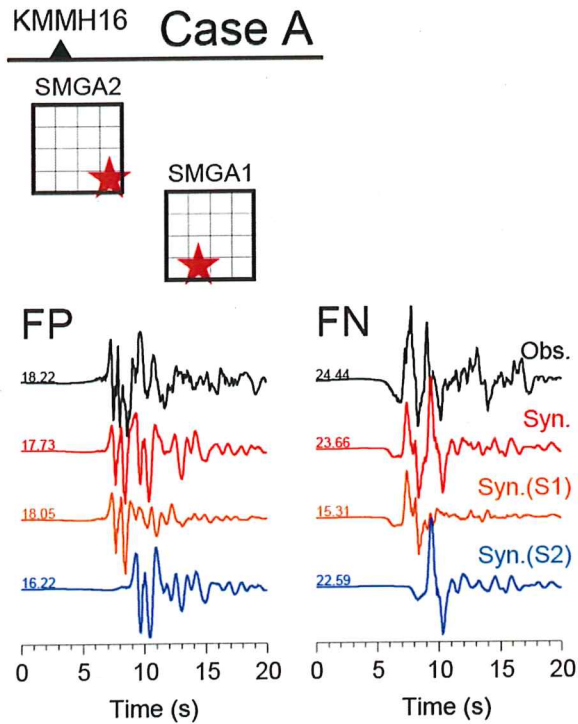
Figure 9

Bird's eye view of the source model for the M7.3 event. Red rectangles of the kinematic inversion model by Yoshida et al. (2017) represent the SMGAs by Irikura et al. (2017). The rupture starting point of each SMGA is indicated by a red star. Black squares show the strong motion stations with observed (black) and simulated (red) acceleration and velocity waveforms in the E–W component (0.2–10 Hz). The maximum amplitude of the waveforms is shown above each trace in cm/s² and cm/s, respectively

For both the M6.5 and M7.3 events, the observed large velocity waveforms in the FP and FN components were better explained by the simulations of Case A compared to those of Case B. This type of up-dip rupture directivity (which hereafter we call "upward directivity") as shown in Case A caused constructive interference of the radiated waves from the strike-slip SMGA to the FP ground motions near the source fault (e.g., Miyatake, 2000). Figure 10a shows that the upward rupture directivity effect from SMGA1 and 2 caused two large FP wave packets for

the M6.5 event. Figure 10b shows that the observed strong pulse in the FP component during the M7.3 event was well explained by the simulation generated from SMGA2 in Case A, which is a typical case implying the upward rupture directivity effect.

However, mechanisms generating strong pulses observed in the FN component were different for the M6.5 and M7.3 events. The two large FN wave-packets during the M6.5 event were generated by the forward rupture directivity effects of SMGA1 and 2 with strike-slip on the vertical fault; the rupture inside

(a) M6.5 KMMH16 downhole (Velocity)

(b) M7.3 KMMH16 downhole (Velocity)
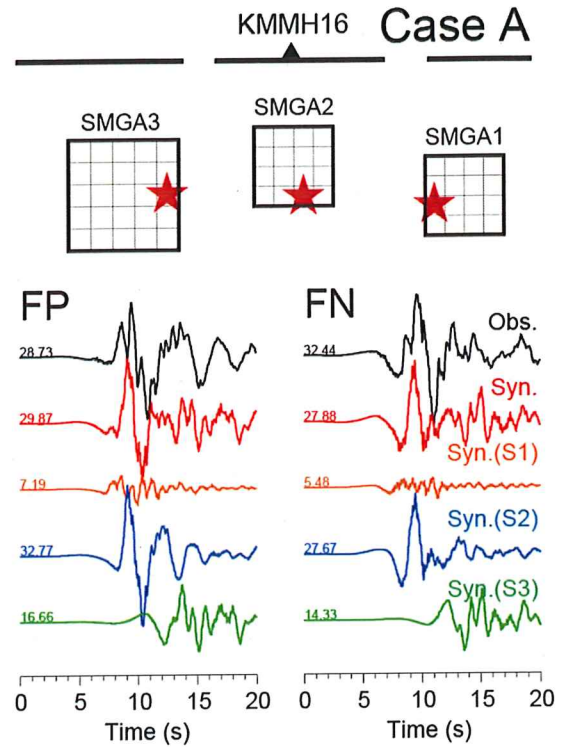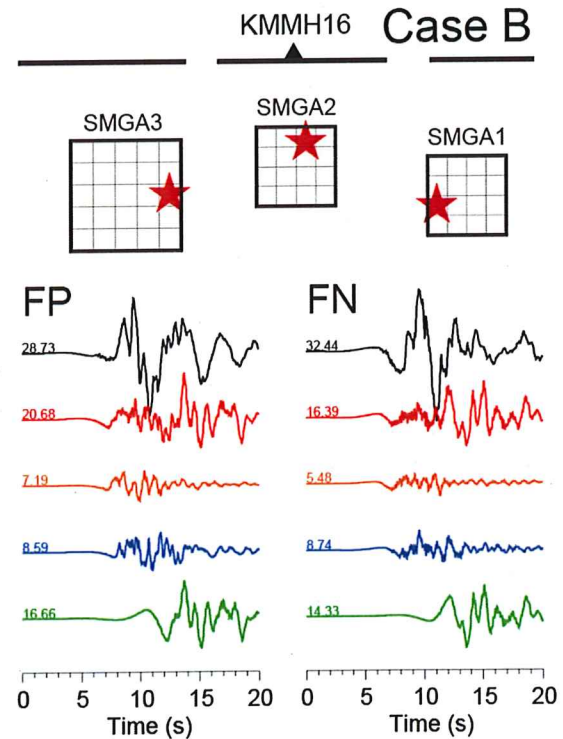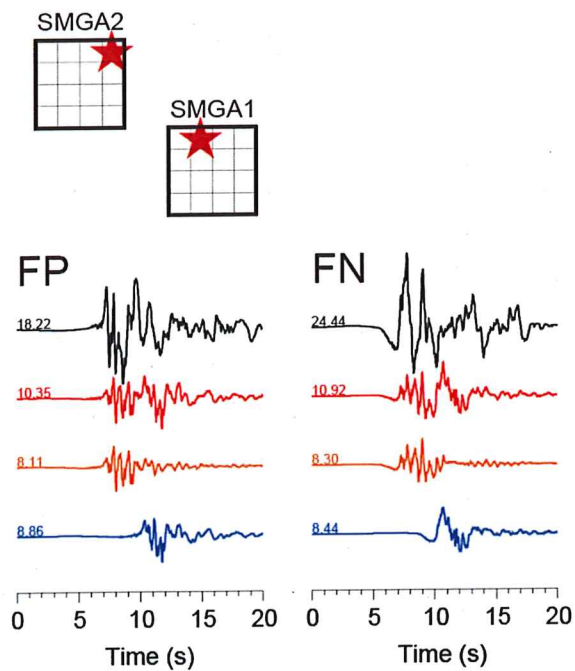
Comparisons between the observed (black) and simulated (red) velocity waveforms in the FP and FN components for the downhole sensor at KMMH16 during the *M*6.5 event (**a**) and the *M*7.3 event (**b**). Orange, blue, and green lines represent the simulations for SMGA1, 2, and 3, respectively. The maximum amplitude of the waveforms is shown above each trace in cm/s. A star indicates the rupture starting point of each rupture case

SMGA1 and 2 propagated in a northeast direction along the fault strike toward KMMH16 from the hypocenter. This type of "forward rupture directivity effect," generating strong pulses in the FN component, has also been observed during past large strike-slip inland crustal earthquakes (e.g., the 1992 Landers earthquake: Somerville et al. 1997; the 1995 Kobe earthquake: Kamae and Irikura 1998). However, the forward rupture directivity is not effective at KMMH16 during the *M*7.3 event because the rupture inside the SMGA, immediately beneath the KMMH16 site, mainly propagated in an upward direction. Therefore, we have to consider another mechanism generating an FN velocity pulse at KMMH16 during the *M*7.3 event.

4.2. Parametric Study Using Hypothetical Source Models

For understanding the forward and upward rupture directivity effects on ground motions in the FN and FP components at the near-source sites, we calculated synthetic ground motions considering the three hypothetical simple source models with the same seismic moment, size, position, and fault geometry, but with different rupture starting points and rake angles (Fig. 11). The source parameters assumed in these source models are summarized in Table 6. The ground motion simulations were performed using the discrete wavenumber method (Bouchon 1981) with the reflection and transmission matrix method (Kennett and Kerry 1979). The underground structure model used in this simulation was assumed to be a simple layered half-space medium, described as a P-wave velocity of 6.0 km/s, S-wave velocity of 3.4 km/s, density of 2.75 kg/m^3, and Q value of 300. The calculation points were set on the ground surface distributed in area of 20×20 km spacing every 1 km for each direction, including the source fault.

The spatial distributions of the peak horizontal ground velocity (PGV) bandpass-filtered between 0.1 and 3 Hz at the ground surface obtained in the ground motion simulations are shown in Fig. 12. Figure 13 also shows the synthetic velocity waveforms from 0.1 to 3.0 Hz at the sites along the fault strike. In Case 1, the unilateral rupture propagation showed stronger FN motions relative to FP motions along the fault trace; in particular, the strongest motion appeared in the FN component around the terminal point of the fault rupture because of the forward rupture directivity effect from the strike-slip fault. This result represented the strong pulse in the FN component observed at KMMH16, the edge of the fault trace, during the *M*6.5 event. In Case 2, the ground motion
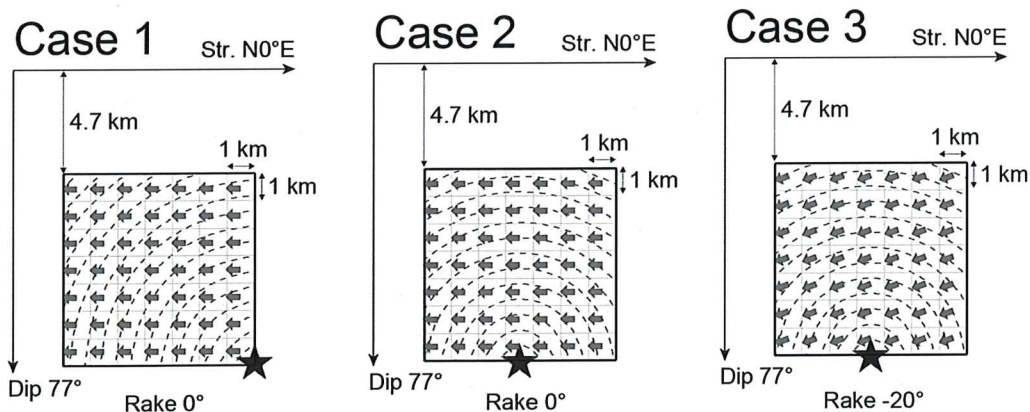

Figure 11
Source models used in strong ground motion simulations from 0.1 to 3.0 Hz. The contour interval of rupture time is 0.2 s. A star indicates the rupture starting point. The gray arrows show slip directions of the hanging wall relative to the footwall

Table 6

Source variables used in the strong motion simulation

		Case 1	Case 2	Case 3
Length	L (km)	7.0	7.0	7.0
Width	W (km)	7.0	7.0	7.0
Area	S (km^2)	49.0	49.0	49.0
Top depth	H (km)	4.7	4.7	4.7
Seismic moment	M_0 (Nm)	2.0×10^{18}	2.0×10^{18}	2.0×10^{18}
Strike	Str. (deg.)	0	0	0
Dip	Dip (deg.)	77	77	77
Rake	Rak. (deg.)	0	0	-20
Rise time	τ (s)	1.2	1.2	1.2
Average slip	D (m)	1.3	1.3	1.3
Rupture velocity	V_r (km/s)	2.8	2.8	2.8
Rupture starting point	–	North-bottom	Center-bottom	Center-bottom
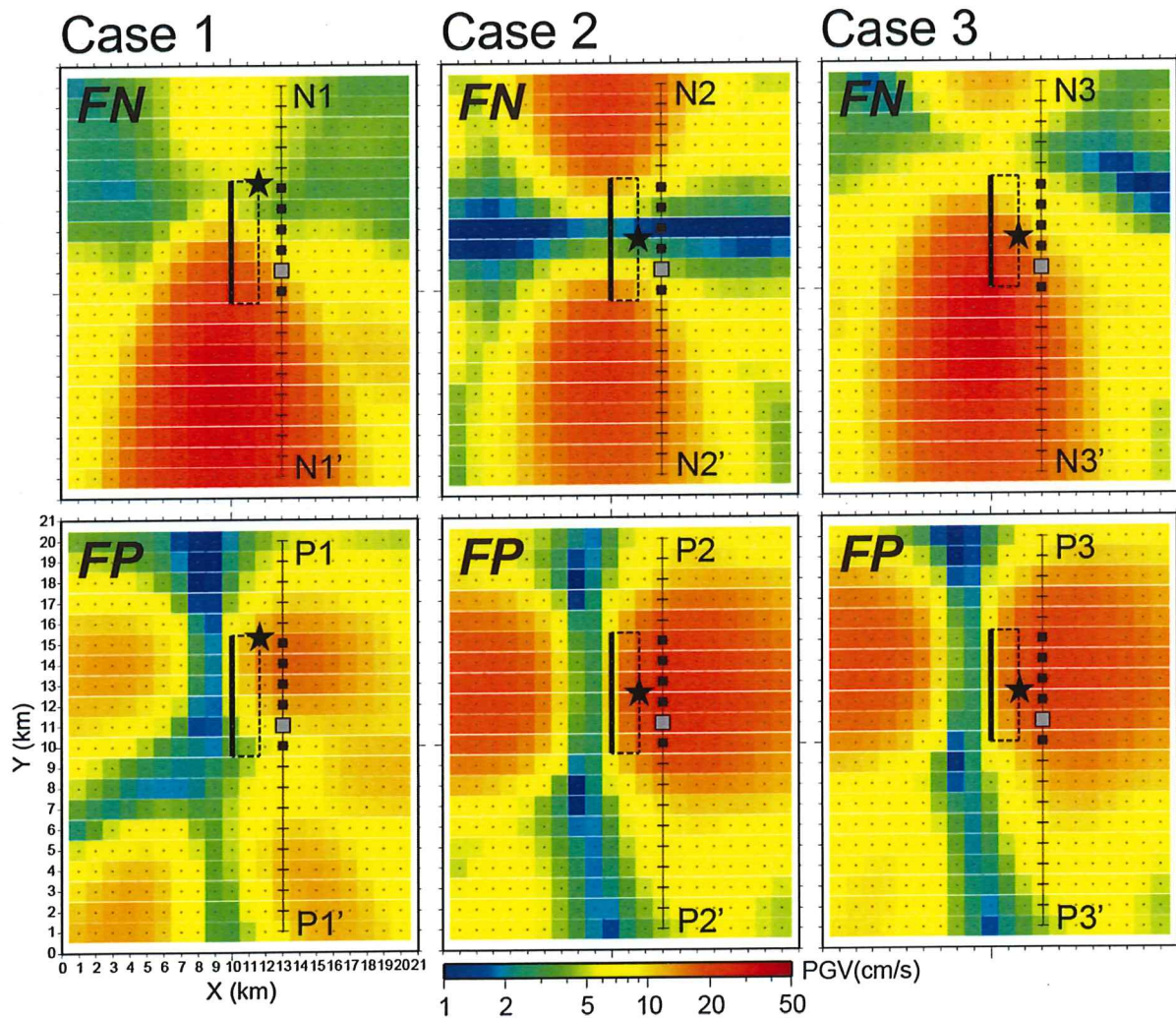
Figure 12
Peak ground velocities on the ground surface predicted in the strong ground motion simulations for Cases 1 (left), 2 (middle), and 3 (right).
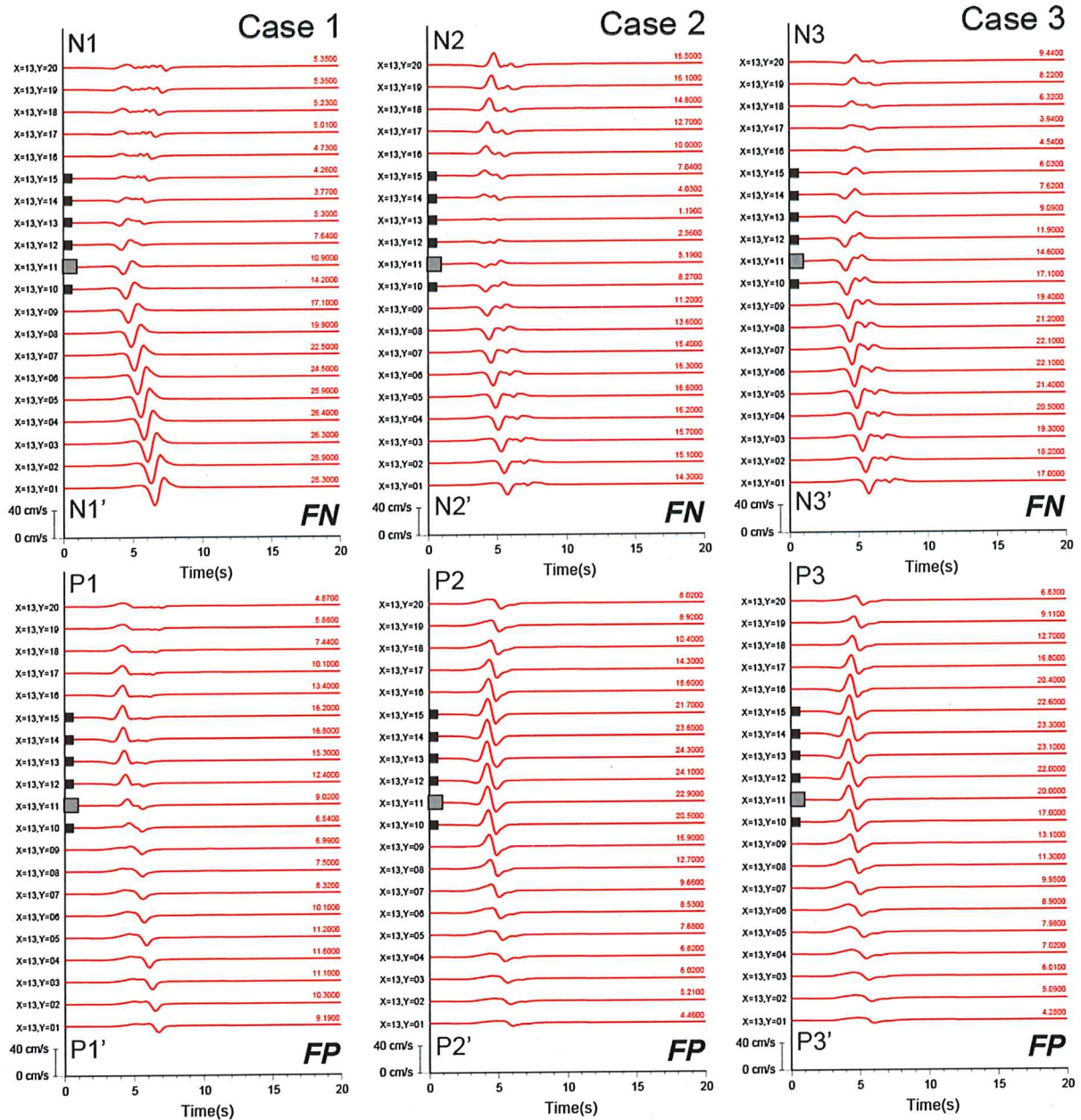Upper panels: FN component. Lower panels: FP component

Figure 13
Simulated velocity waveforms from 0.1 to 3.0 Hz. Solid squares on the waveform traces indicate the site points shown in Fig. 12. The maximum amplitude of the observed waveform is shown above each trace in cm/s. The gray solid square point is the assumed location of station KMMH16

near the center of the fault trace was stronger in the FP component than that in the FN component. This was caused by the upward directivity effect from the strike-slip fault. However, the strong pulse at KMMH16 during the $M7.3$ event was also observed in the FN component as well as in the FP component.

To explain this observation in terms of the source model, we tried to simulate it in Case 3, which had same source parameters as Case 2 except for the rake angle on the fault; the rake angle in case 3 was set to be $-20°$, which is a left lateral strike-slip with a small normal fault slip, while that in Cases 1 and 2

*M*7.3 event
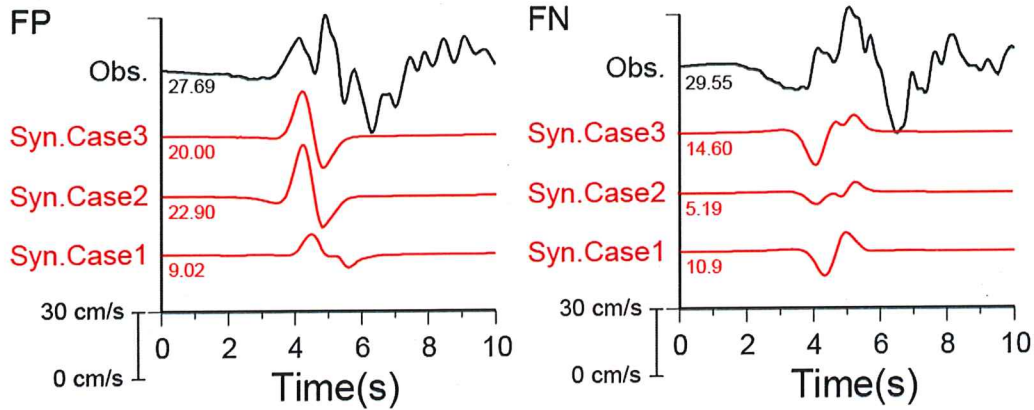### KMMH16 downhole (Velocity 0.1-3.0 Hz)

Figure 14

Comparisons of velocity waveforms in the FP (left) and FN (right) components at KMMH16 during the *M*7.3 event between observation (black) and synthetic velocity waveforms (red) from 0.1 to 3.0 Hz for Cases 1, 2, and 3. The maximum amplitude of the waveforms is shown below each trace in cm/s

was 0°. The simulated ground motions near the center of the fault trace in Case 3 showed a high PGV for both the FP and FN components.

Figure 14 shows the synthetic waveforms comparing to the observed waveforms at the KMMH16 station during the *M*7.3 event. The synthetic waveforms in Case 3 are in better agreement with the observed waveforms for both the FP and FN components than those in Cases 1 and 2. These results from ground motion simulations suggest the strong pulses in the FP and FN components at KMMH16 during the *M*7.3 event were caused by the upward rupture directivity effect from the strike-slip fault with a small normal slip. Notably, the geometry of the fault (strike and dip) near KMMH16 is one of the key parameters in discussing the difference in ground motion between the FP and FN components. However, the oblique slip direction in and around SMGA2 also appeared in the heterogeneous slip model inferred from the kinematic waveform inversions for the *M*7.3 event as shown in Fig. 8.

5. Conclusions

We conducted strong ground motion simulations based on the SMGA source models for two large *M*6.5 and *M*7.3 events of the 2016 Kumamoto earthquakes. Strong ground motion simulations were performed in a broadband frequency range between 0.2 and 10 Hz using the EGF method. For the *M*6.5 event, two squared SMGAs near the large slip areas of the kinematic inversion source model were estimated by forward modeling through ground motion simulations. For the *M*7.3 event, the three-SMGA model on the multi-segment fault model constructed by Irikura et al. (2017) was used for ground motion simulations. These SMGA models for both the *M*6.5 and *M*7.3 events were able to reproduce well the characteristics of the observed ground motions in and around the source areas, including the strong velocity pulses observed at the near-source station KMMH16. From the parametric studies through the ground motion simulations, we concluded that the mechanisms generating the strong pulses at KMMH16 during the *M*6.5 and *M*7.3 events were as follows: For the *M*6.5 event, the forward and upward rupture directivity from the SMGA caused the strong pulses in the FN and FP components. For the *M*7.3 event, the upward rupture directivity along the fault dip direction from the SMGA with strike-slip including small normal slip, immediately beneath KMMH16, caused the strong pulse in both the FP and FN components. These rupture directivity effects are quite

important in estimating and predicting the near-source strong ground motions for inland crustal earthquakes.

Publisher's Note Springer Nature remains neutral with regard to jurisdictional claims in published maps and institutional affiliations.

References

Aoi, S., Kunugi, T., Nakamura, H., & Fujiwara, H. (2011). Deployment of new strong motion seismographs of K-NET and KiK-net. In S. Akkar, P. Gülkan, & T. van Eck (Eds.), *Earthquake data in engineering seismology: geotechnical, geological, and earthquake engineering* (Vol. 14, pp. 167–168). Dordrecht: Springer.

Asano, K., & Iwata, T. (2016). Source rupture processes of the foreshock and mainshock in the 2016 Kumamoto earthquake sequence estimated from the kinematic waveform inversion of strong motion data. *Earth, Planets and Space, 68,* 147. https://doi.org/10.1186/s40623-016-0519-9.

Bouchon, M. (1981). A simple method to calculate Green's functions for elastic layered media. *Bulletin of the Seismological Society of America, 71,* 959–971.

Fire and Disaster Management Agency. (2018). The 2016 Kumamoto earthquake (111th report), http://www.fdma.go.jp/bn/2016/detail/960.html. Accessed 20 Feb. 2018 (in Japanese).

Fujiwara, H., Kawai, S., Aoi, S., Morikawa, N., Senna, S., Azuma, H., et al. (2012). Some improvements of seismic hazard assessment based on the 2011 Tohoku earthquake. *Technical Note of the National Research Institute for Earth Science and Disaster Prevention, 379.*

Fujiwara, H., Kawai, S., Aoi, S., Morikawa, N., Senna, S., Kudo, N., et al. (2009). A Study on subsurface structure model for deep sedimentary layers of Japan for strong-motion evaluation. *Technical Note of the National Research Institute for Earth Science and Disaster Prevention, 337.*

Fujiwara, S., Yarai, H., Kobayashi, T., Morishita, Y., Nakano, T., Miyahara, B., et al. (2016). Small-displacement linear surface ruptures of the 2016 Kumamoto earthquake sequence detected by ALOS-2 SAR interferometry. *Earth, Planets and Space, 68,* 160. https://doi.org/10.1186/s40623-016-0534-x.

Fukuyama, E., Ishida, M., Dreger, D. S., & Kawai, H. (1998). Automated seismic moment tensor determination using on-line broadband seismic waveforms. *Zisin (Journal of the Seismological Society of Japan), 2*(51), 149–156. **(In Japanese with English abstract).**

Hao, J., Ji, C., & Yao, Z. (2017). Slip history of the 2016 M_w 7.0 Kumamoto earthquake: Intraplate rupture in complex tectonic environment. *Geophysical Research Letters, 44,* 743–750.

Irikura, K. (1986). Prediction of strong acceleration motions using empirical Green's function. In: Proceedings of the 7th Japan Earthquake Engineering Symposium, Tokyo, 151–156.

Irikura, K., Kagawa, T., & Sekiguchi, H. (1997). Revision of the empirical Green's function method by Irikura (1986), programme and abstracts. *Seismological Society of Japan, 69,* B25. **(In Japanese).**

Irikura, K., Miyakoshi, K., Kamae, K., Yoshida, K., Somei, K., Kurahashi, S., et al. (2017). Applicability of source scaling relations for crustal earthquakes to estimation of the ground motions of the 2016 Kumamoto earthquake. *Earth, Planets and Space, 69,* 10. https://doi.org/10.1186/s40623-016-0586-y.

Kamae, K., & Irikura, K. (1998). Source model of the 1995 Hyogo–Ken Nanbu earthquake and simulation of near-source ground motion. *Bulletin of the Seismological Society of America, 88,* 400–412.

Kato, A., Fukuda, J., Nakagawa, S., & Obara, K. (2016). Foreshock migration preceding the 2016 M_w 7.0 Kumamoto earthquake, Japan. *Geophysical Research Letters, 43,* 8945–8953.

Kennett, B. L. M., & Kerry, N. J. (1979). Seismic waves in a stratified half space. *Geophysical Journal of the Royal Astronomical Society, 57,* 557–583.

Kobayashi, H., Koketsu, K., & Miyake, H. (2017a). Rupture processes of the 2016 Kumamoto earthquake sequence: Causes for extreme ground motions. *Geophysical Research Letters, 44,* 6002–6010.

Kobayashi, G., Mamada, Y., & Wu, C. (2017b). Analysis of the factors of large acceleration amplitude and estimation of the bedrock ground motions at the KiK-net Mashiki station caused by the maximum foreshock (M_j 6.5) of the 2016 Kumamoto

earthquakes. *Journal of Japan Association for earthquake engineering, 17–4,* 101–139. **(In Japanese with English abstract).**

Kubo, H., Suzuki, W., Aoi, S., & Sekiguchi, H. (2016). Source rupture processes of the 2016 Kumamoto, Japan, earthquakes estimated from strong-motion waveforms. *Earth, Planets and Space, 68,* 161. https://doi.org/10.1186/s40623-016-0536-8.

Kurita, T. (2017). Nonlinearity amplification of subsurface ground at KiK-net Mashiki site during the 2016 Kumamoto earthquake. *Journal of civil engineering A1(structure/earthquake engineering), 73,* 74–82. **(In Japanese, abstract in English).**

Miyake, H., Iwata, T., & Irikura, K. (2003). Source characterization for broadband ground-motion simulation: Kinematic heterogeneous source model and strong motion generation area. *Bulletin of the Seismological Society of America, 93,* 2531–2545.

Miyatake, T. (2000). Computer simulation of strong ground motion near a fault using dynamic fault rupture modeling: Spatial distribution of the peak ground velocity vectors. *Pure and Applied Geophysics, 157,* 2063–2081.

Nakata, T., & Imaizumi, T. (Eds.). (2002). *Digital active fault map of Japan*. Tokyo: University of Tokyo Press.

Ozawa, T., Fujita, E., & Ueda, H. (2016). Crustal deformation associated with the 2016 Kumamoto Earthquake and its effect on the magma system of Aso volcano. *Earth, Planets and Space, 68,* 186. https://doi.org/10.1186/s40623-016-0563-5.

Satoh, T. (2016). Source, path and site effects of the 2016 Kumamoto earthquake, the foreshocks and aftershocks using the spectral inversion method. In: Abstracts of Japan Geoscience Union Meeting 2016, MIS3-P71.

Shirahama, Y., Yoshimi, M., Awata, Y., Maruyama, T., Azuma, T., Miyashita, Y., et al. (2016). Characteristics of the surface ruptures associated with the 2016 Kumamoto earthquake sequence, central Kyushu, Japan. *Earth, Planets and Space, 68,* 191. https://doi.org/10.1186/s40623-016-0559-1.

Si, H., & Midorikawa, S. (1999). New attenuation relationships for peak ground acceleration and velocity considering effects of fault type and site condition. *Journal of Structural and Construction Engineering, 523,* 63–70. **(In Japanese with English abstract).**

Somerville, P. G., Smith, N. F., Graves, R. W., & Abrahamson, N. A. (1997). Modification of empirical strong ground motion attenuation relations to include the amplitude and duration effects of rupture directivity. *Seismological Research Letters, 68,* 199–222.

Sugito, N., Goto, H., Kumahara, Y., Tsutsumi, H., Nakata, T., Kagohara, K., et al. (2016). Surface fault ruptures associated with the 14 April foreshock (M_j 6.5) of the 2016 Kumamoto earthquake sequence, southwest Japan. *Earth Planets and Space, 68,* 170. https://doi.org/10.1186/s40623-016-0547-5.

Suzuki, W., Aoi, S., Kunugi, T., Kubo, H., Morikawa, N., Nakamura, H., et al. (2017). Strong motions observed by K-NET and KiK-net during the 2016 Kumamoto earthquake sequence. *Earth, Planets and Space, 69,* 19. https://doi.org/10.1186/s40623-017-0604-8.

Uchide, T., Horikawa, H., Nakai, M., Matsushita, R., Shigematsu, N., Ando, R., et al. (2016). The 2016 Kumamoto–Oita earthquake sequence: aftershock seismicity gap and dynamic triggering in volcanic areas. *Earth, Planets and Space, 68,* 180. https://doi.org/10.1186/s40623-016-0556-4.

Wessel, P., & Smith, W. H. F. (1998). New, improved version of Generic Mapping Tools released. *Eos Transaction American Geophysical Union, 79,* 579.

Yagi, Y., Okuwaki, R., Enescu, B., Kasahara, A., Miyakawa, A., & Otsubo, M. (2016). Rupture process of the 2016 Kumamoto earthquake in relation to the thermal structure around Aso volcano. *Earth, Planets and Space, 68,* 118. https://doi.org/10.1186/s40623-016-0492-3.

Yoshida, K., Miyakoshi, K., & Somei, K. (2016). Source processes of three large events of the 2016 Kumamoto earthquakes inferred from waveform inversion with strong-motion records. In: Abstracts of Japan Geoscience Union Meeting 2016, MIS34-P64.

Yoshida, K., Miyakoshi, K., Somei, K., & Irikura, K. (2017). Source process of the 2016 Kumamoto earthquake (M_j7.3) inferred from kinematic inversion of strong-motion records. *Earth Planets and Space, 69,* 64. https://doi.org/10.1186/s40623-017-0649-8.